Title

Statistical 3D morphology characterization of vaterite microspheres produced by engineered Escherichia coli

Authors

Lin, Alex YW

Wu, Zong-Yen

Pattison, Alexander J

et al.

Publication Date

2024

DOI

10.1016/j.bioadv.2023.213711

Statistical 3D Morphology Characterization of Vaterite Microspheres Produced by Engineered *Escherichia coli*

Alex Y. W. Lin [a], Zong-Yen Wu [b], Alexander J. Pattison [a], Isaak E. Müller [b], Yasuo Yoshikuni [b], Wolfgang Theis [c], Peter Ercius [a] *

[a] National Center for Electron Microscopy, Molecular Foundry, Lawrence Berkeley National Laboratory, Berkeley, CA 94720, USA
[b] US Department of Energy Joint Genome Institute, Lawrence Berkeley National Laboratory, Berkeley, CA 94720, USA
[c] Nanoscale Physics Research Laboratory, School of Physics and Astronomy, University of Birmingham, Edgbaston, Birmingham B15 2TT, UK

* Corresponding author: Peter Ercius
email: percius@lbl.gov
postal address: 1 Cyclotron Road, MS 72-150, Berkeley, CA 94720 USA

Abstract

Hollow vaterite microspheres are important materials for biomedical applications such as drug delivery and regenerative medicine owing to their biocompatibility, high specific surface area, and ability to encapsulate a large number of bioactive molecules and compounds. We demonstrated that hollow vaterite microspheres are produced by an *Escherichia coli* strain engineered with a urease gene cluster from the ureolytic bacteria *Sporosarcina pasteurii* in the presence of bovine serum albumin. We characterized the 3D nanoscale morphology of five biogenic hollow vaterite microspheres using 3D high-angle annular dark field scanning transmission electron microscopy (HAADF-STEM) tomography. Using automated high-throughput HAADF-STEM imaging across several sample tilt orientations, we show that the microspheres evolved from a smaller more ellipsoidal shape to a larger more spherical shape while the internal hollow core increased in size and remained relatively spherical, indicating that the microspheres produced by this engineered strain likely do not contain the bacteria. The statistical 3D morphology information demonstrates the potential for using biogenic calcium carbonate mineralization to produce hollow vaterite microspheres with controlled morphologies.

Keywords: Vaterite, Scanning transmission electron microscopy, 3D morphology, Biomineralization, MICP

Statement of Significance

The nanoscale 3D structures of biomaterials determine their physical, chemical, and biological properties, however significant efforts are required to obtain a statistical understanding of the internal 3D morphology of materials without damaging the structures. In this study, we developed a non-destructive, automated technique that allows us to understand the nanoscale 3D morphology of many unique hollow vaterite microspheres beyond the spectroscopy methods that lack local information and microscopy methods that cannot interrogate the full 3D structure. The method allowed us to quantitatively correlate the external diameters and aspect ratios of vaterite microspheres with their hollow internal structures at the nanoscale. This work demonstrated the opportunity to use automated transmission electron microscopy to characterize nanoscale 3D morphologies of many biomaterials and validate the chemical and biological functionality of these materials.

Graphical Abstract

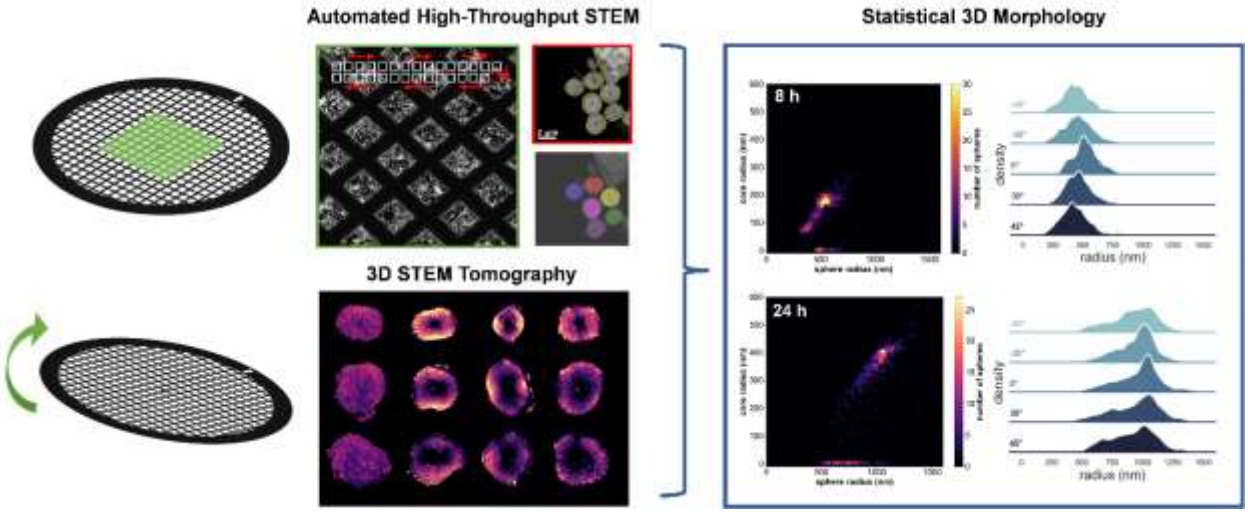

1. Introduction

Nature is replete with biogenic materials that have complex hierarchical structures with precise organic-inorganic components, crystal morphology, and chemical composition over multiple length scales [1]. These biologically produced materials have unique mechanical, magnetic, or optical properties for various biological functions and are typically produced by organisms at ambient conditions. As the sustainable production of advanced materials for a wide range of applications continues to gain considerable interest, recent efforts have focused on mimicking biomineralization in vitro using a variety of biomolecules such as proteins and peptides to build functional inorganic materials and modulate the assembly process during mineralization. Calcium carbonate ($CaCO_3$), which is the one of the most abundant biogenic materials used by organisms to grow hard structures, has been a model for understanding the pathways of biomineralization. Biogenic $CaCO_3$ has three crystalline polymorphs: calcite, aragonite, and vaterite. While calcite is the most abundant in nature due to its thermodynamic stability, vaterite, which is a metastable polymorph, has a wide range of applications such as drug delivery [2–6], regenerative medicine [7,8], and water remediation [9,10]. While uncommon due to its thermodynamic instability and high solubility in water, vaterite is synthesized by and can persist in several biological sources such as hard mineralized tissues [11–14] and geological environments [15–17]. There have also been numerous studies on vaterite synthesis by using biomolecule additives [18–22] or templates [23–26] to control the polymorphic nature of $CaCO_3$ and stabilize the vaterite phase. Additionally, several other studies have shown that vaterite can be synthesized by altering precipitation conditions such as pH and the degree of supersaturation in the solution [27–29].

While there are many pathways to precipitate $CaCO_3$, microbially induced calcium carbonate precipitation (MICP) is a potential route to facile synthesis controlled by a microbial metabolic process that creates a local microenvironment with favorable conditions for precipitation of carbonate minerals. One mechanism of MICP is the biogenic formation of $CaCO_3$ via urea hydrolysis, a process in which the urease enzyme hydrolyzes urea to form ammonia and carbamic acid, which then hydrolyzes to ammonia and carbonic acid. Ureolytic microorganisms such as the soil bacterium *Sporosarcina pasteurii* (*S. pasteurii*) produce the urease enzyme and are efficient at the mineralization of $CaCO_3$ [30]. The pH, calcium ion (Ca^{2+}) concentration, and dissolved inorganic carbon concentration, which are affected by the ureolytic activity of the microorganism, dictate the precipitation conditions of $CaCO_3$.

Recent studies have shown that MICP in ureolytic microorganisms can control the crystal size and morphology of $CaCO_3$ precipitates by engineering *Escherichia coli* (*E. coli*) with the urease gene cluster from *S. pasteurii* [31,32]. Additionally, microbially precipitated vaterite has been observed previously in the presence of *Myxococcus xanthus* [33,34] and also in an *E. coli* strain engineered with the urease gene cluster [35], suggesting that MICP can also modulate the polymorphic nature of $CaCO_3$ and tailor the material properties of these crystal precipitates. While previous studies characterized the crystal size and morphology of microbially precipitated $CaCO_3$ using techniques such as X-ray diffraction, Fourier transform infrared (FTIR) spectroscopy and Raman spectroscopy, the results often provide a limited understanding of the nanoscale morphological features due to their bulk-scale perspective. Electron microscopy such as scanning electron microscopy and transmission electron microscopy (TEM) have provided more local information but lack the ability to interrogate the full 3D structure. Furthermore, studies that probe the 3D structure of vaterite use destructive techniques such as ion milling [34] or focused ion beam milling [35] which can alter particle morphology. Since vaterite typically forms polycrystalline spherical particles, often referred to as microspheres or spherulites, that can be either hollow or solid, large-scale 3D morphological information is crucial for understanding the biomineralization pathways for producing vaterite particles with different geometries.

Here we present a method to precipitate large quantities of hollow vaterite microspheres using an *E. coli* strain engineered with a urease gene cluster with bovine serum albumin (BSA) added to the culture media. To characterize the nanoscale 3D morphology and visualize the outer and inner surfaces of these vaterite microspheres, we performed HAADF-STEM tomography on several of these microspheres. We additionally expanded the abilities of automated HAADF-STEM imaging [36,37] by acquiring images with ~15 nm resolution from a large region of interest (360 µm x 360 µm) at several different projection orientations, enabling the collection of 3D particle size and morphology from a large population of vaterite microspheres. Finally, we use this statistical 3D morphology data to compare the vaterite microspheres at two different growth times and infer crystal growth dynamics in order to further understand how to precisely control crystal morphology using microbial precipitation.

2. Methods and Materials

2.1 Strains and culture conditions used for vaterite synthesis

We used an *E. coli* ATCC8739 strain expressing the urease gene cluster from *Sporosarcina pasteurii* ATCC 11859 for vaterite synthesis (manuscript in preparation). Vaterite synthesis was performed semi-aerobically using a urea-$CaCl_2$ medium [31], which contained 20 g/L urea, 3 g/L LB broth, 0.65 mg/L $NiCl_2$, and 5.6 g/L $CaCl_2$ supplemented with or without 10 g/L of bovine serum albumin (BSA). The pH was adjusted for the final pH 6.0 using 6N HCl. The synthesis was carried out by using Thermo Scientific Cimarec i Telesystem stirrer in a water bath at 30 °C with 200 rpm stirring and a starting OD of 0.1 for 8 h (with BSA) and 24 h (with and without BSA). The vaterite precipitates were collected with Whatman Grade 50 quantitative filter papers.

2.2 Transmission Electron Microscopy

Crystal precipitates were dispersed in distilled water and deposited onto lacey carbon 300 mesh copper grids. TEM imaging and selected-area electron diffraction (SAED) were performed on a Thermo Fisher ThemIS TEM equipped with an X-FEG gun operating at 300 kV with a Ceta2 complementary metal oxide semiconductor (CMOS) camera. HAADF-STEM images were acquired at 300 kV with a convergence semi-angle of 11.3 mrad. To determine the compositions of the crystals, energy dispersive X-ray spectroscopy (EDX) was performed using a Bruker SuperX windowless EDX detector, which has a solid angle of 0.7 steradian enabling high count rates with minimal dead time for fast STEM-EDX mapping. STEM-EDX elemental mapping was performed at 300 kV with a beam current of 200 pA over a 5 min acquisition time.

2.3 STEM Tomography

The tomography experiment was performed using a Thermo Fisher ThemIS microscope operated at 300 kV [38]. The HAADF-STEM images were acquired with a 11.3 mrad probe convergence semi-angle. The projections of the vaterite spheres were recorded over the tilt range of −70° to 70°, with 2° step size and a pixel size of 5.5 nm. The tilt series was aligned and reconstructed with the simultaneous iterations reconstruction technique (SIRT) algorithm using the IMOD tomography package [39]. Then, volume rendering and visualization was performed using Tomviz 1.10.0 [40].

2.4 Automated High-Throughput STEM

Automated high-throughput STEM data was acquired using a Thermo Fisher

aberration corrected Titan 80-300 (TEAM 0.5) microscope and the all-piezo driven TEAM stage [41] at the National Center for Electron Microscopy facility of the Molecular Foundry at Lawrence Berkeley National Laboratory. Images were acquired at 300 kV in HAADF-STEM mode with a 30 mrad probe convergence semi-angle and 61 and 210 mrad detector inner and outer semi-angles, respectively. Automated data acquisition was controlled by a custom microscope control software (Wtip and server software) [37], which controlled the stage positions and performed automatic focusing during data acquisition. For both 8 h growth and 24 h growth samples, high-throughput STEM data was acquired at 5 different tilt angles, -45°, -30°, 0°, 30°, and 45°, with a pixel size of 7.65 nm. At 0° tilt, a full dataset consisting of 23 x 23 HAADF-STEM images (total of 529 images) was acquired for each sample. The acquisition time for the 23 x 23 image dataset was approximately 6.5 h. At the other tilt angles, datasets were acquired starting from the upper right corner of the same region as the first image of the 0° tilt dataset to ensure identical regions are collected at all tilt angles. The region of interest compresses normal to the tilt axis making the total projected area of the target region smaller at higher tilt angles. Thus, the non-zero tilt angle datasets were acquired until the entire region covered by the 0° tilt dataset was imaged, resulting in datasets with 300 to 500 total images depending on tilt angle.

2.5 Data Analysis

The radii and aspect ratios of the vaterite spheres were measured using image segmentation and region property measurement functions from the scikit-image Python package. In order to determine the thicknesses of the hollow vaterite spheres, a cubic function was fitted to radial sums of HAADF-STEM image intensities, which are directly proportional to specimen thickness, using the scipy Python package (see SI). Due to the projection nature of STEM imaging, we cannot directly measure the 3D diameter of individual hollow structures. Instead, the first maxima of the cubic functions fitted to the radial sum, which approximately determined the location of the densest projected part of the vaterite spheres, were used to measure the extent of the internal cavity from the center of the spheres. This measurement was then used as an estimate of the sizes of the hollow cores. 2D cross-correlation was performed on images across all tilt angles for each sample using the scipy Python package to locate the same sample regions across different stage tilt angles. Image correlation matches were verified by eye, and the corresponding morphology measurements for correct matches were used to quantify morphological changes with respect to angular orientation. Few regions could be analyzed in this way due to the overlap of many objects at high tilt angles.

3. Results and Discussion

TEM images of $CaCO_3$ synthesized with and without bovine serum albumin (BSA) and with different growth times are shown in Figure 1. $CaCO_3$ synthesized in the presence of 10 g/L of bovine serum albumin (BSA) consists of small vaterite nanoparticles assembled into hollow microspheres. In contrast, $CaCO_3$ synthesized without BSA shows vaterite nanoparticles with no specific assembled structure. The SAED patterns, shown as insets of Figures 1D-F, show polycrystalline diffraction rings that correspond to Bragg reflections for the vaterite $CaCO_3$ polymorph. STEM-EDX of both structures show they consist of Ca, C, and O with similar compositions. From the HAADF-STEM images and STEM-EDX compositional maps in Figure 2, the center of each vaterite microsphere appears to be hollow as electron and X-ray signals observed near the center show lower intensities. This suggests that the microspheres contain a hollow core similar to previous studies of hollow $CaCO_3$ nanoparticles [42–44].

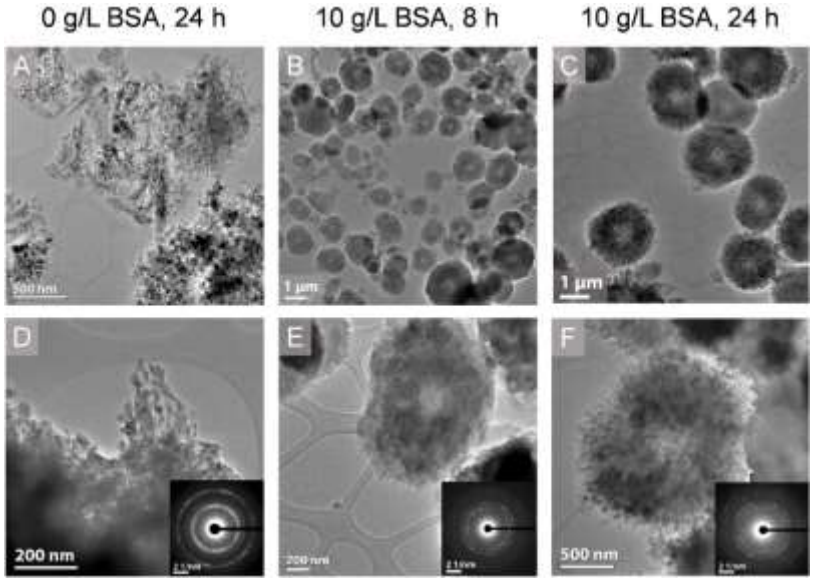

Figure 1. TEM imaging and electron diffraction patterns (inset) of different vaterite structures synthesized by engineered *E. coli*. TEM images of vaterite produced by (A, D) engineered *E. coli* in 24 h, (B, E) engineered *E. coli* with 10 g/L of BSA in 8 h, and (C, F) engineered *E. coli* with 10 g/L of BSA in 24 h.

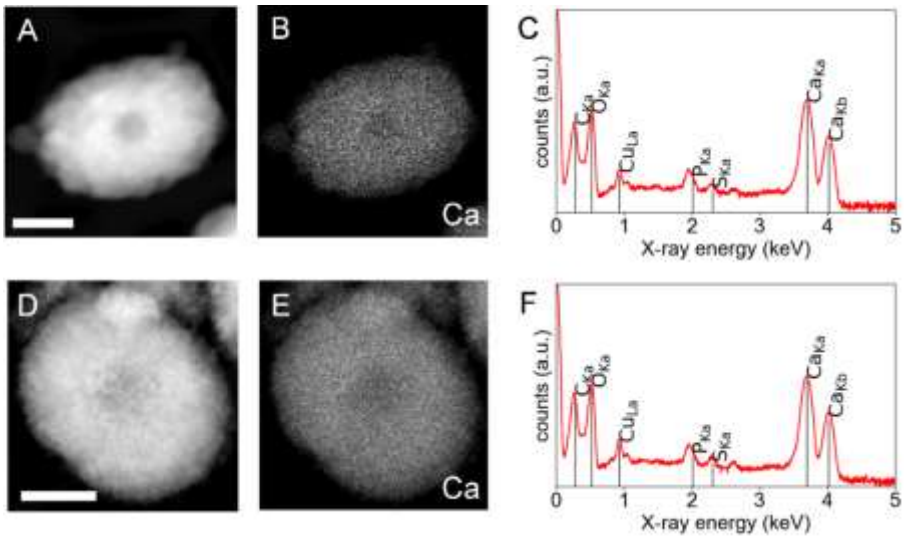

Figure 2. HAADF-STEM imaging and STEM-EDS mapping of vaterite microspheres. (A) HAADF-STEM image of a vaterite microsphere grown for 8 h and (B) the corresponding STEM-EDS map showing Ca distribution. (C) The EDS spectrum primarily shows Ca, C, and O X-ray peaks with minor S and P peaks from the media and Cu peak from the TEM grid. (D) HAADF-STEM imaging of a vaterite microsphere grown for 24 h shows that the structure becomes more round as it grows. (E) The hollow core, indicated by the decrease of Ca X-ray signals, also grew in size although it remained circular. (F) The chemical composition of the 24 h microsphere is very similar to the 8 h one shown in (C). Scale bars, 1 μm.

It is well-established that MICP can produce calcite and vaterite. However there have been limited studies showing the ability to modulate the polymorphic nature and the 3D morphology of calcium carbonate structures using microbial synthesis methods. By demonstrating the formation of vaterite, the engineered *E. coli* strain can replicate the biomineralization functions commonly found in ureolytic bacteria such as *S. pasteurii* [30] and *Myxococcus xanthus* [33,34]. The addition of bovine serum albumin, which has been shown to stabilize the metastable vaterite $CaCO_3$ polymorph [19,21,22], is then used to direct the precipitation of vaterite into hollow microspheres, which have broad biomedical applications. Upon the analysis of the 2D HAADF-STEM images in Figure 1, it is evident that these microspheres have similar outer diameters depending on the growth time. Since hollow vaterite microspheres are materials of interest for drug delivery applications, characterization of the 3D morphology of these structures is crucial for understanding parameters such as loading capacity and biodegradability.

In order to examine the 3D structures of these microspheres, we used HAADF-STEM tomography and 3D reconstructions to reveal the internal structure of the microspheres after 24 h of growth. 3D electron tomography reconstructions as shown in Figure 3 and Supplementary

Movie 1 reveal that the inner and outer surfaces of these vaterite microspheres are irregular and rough at the nanoscale, and most of these microspheres have round, hollow cavities. The reconstructed structures show that most of these microspheres contain an inner cavity that ranges from 300-500 nm in radius. The outer surfaces of the microspheres are not smooth, as they consist of many small vaterite nanoparticles. The inner surfaces of the cavities are also highly irregular although the cavities themselves have a roughly spherical shape. 3D reconstructions of three representative microspheres and orthogonal 5 nm thick cross-sectional slices from the reconstruction centers along each orthogonal direction are shown in Figure 3C.

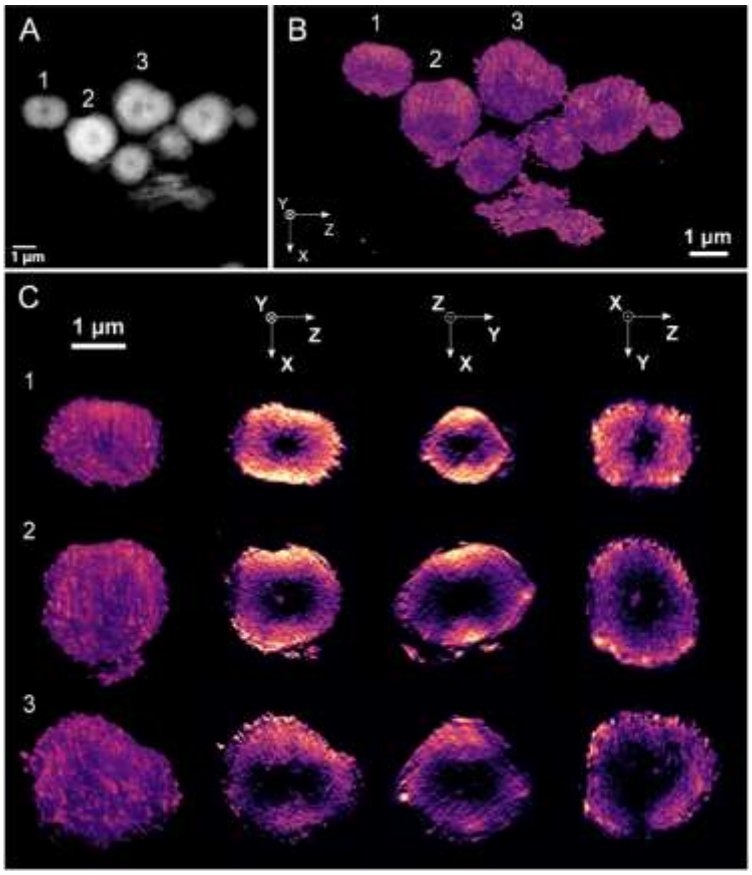

Figure 3. 3D electron tomography reconstruction of vaterite microspheres. (A) HAADF-STEM image of five vaterite microsphere grown for 24 h and (B) the corresponding 3D reconstruction showing the 3D nanoscale structures of the microspheres. (C) 2D orthoslices from all three projections of microspheres labeled (1), (2), and (3) in (A-B) that show the 3D morphology of the hollow cavities can vary even though the microspheres have similar external shapes.

In the first example, the microsphere has an elongated morphology with a hollow center with a radius of 380 nm that is approximately spherical with rough edges as seen in all three cross-sectional views. The second example shows a microsphere with an approximately 1 um radius with a more spherical morphology. The 3D reconstruction as shown in Supplementary Movie 1

revealed a calcite crystal plate on the outer surface of this microsphere. The inner surface is similar to the first example where the hollow cavity is mostly spherical with rough edges; however, the shell of the microsphere has a consistent thickness around the inner cavity in this case. The final example shows an irregularly shaped vaterite sphere with an elongated cavity. Based on the dumbbell-shaped cavity, it is likely that this sphere was created when two smaller hollow microspheres fused together during the growth process.

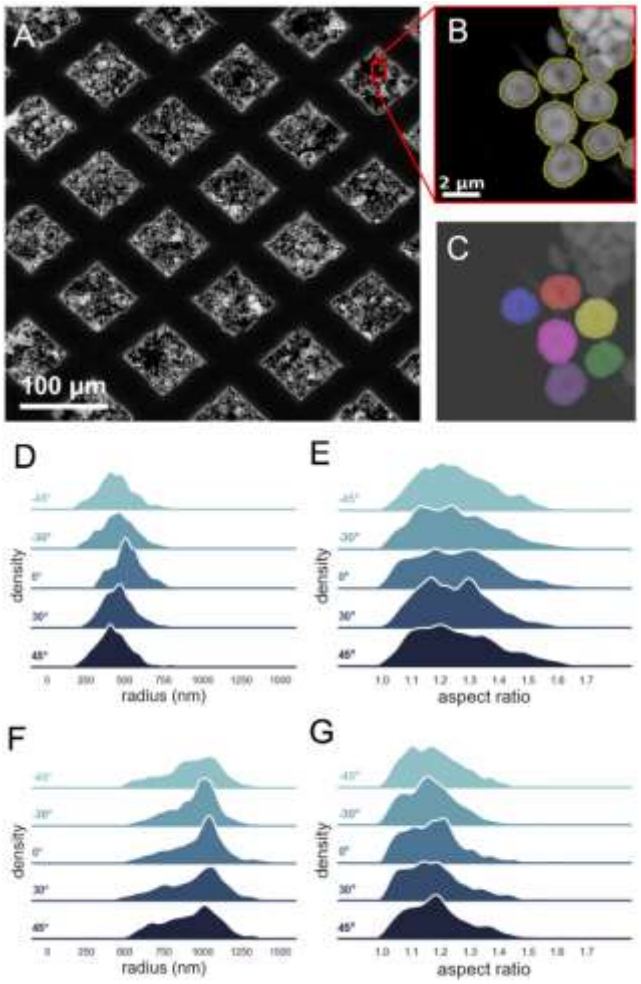

Figure 4. Automated HAADF-STEM combined with image segmentation revealed the morphology of large populations of vaterite microspheres. (A) A montage of 529 HAADF-STEM images of vaterite microsphere grown for 24 h. (B) Each image tile has a spatial resolution of about 15 nm and contains several vaterite microspheres. (C) The vaterite microspheres as seen in (B) were segmented and their projected morphology were measured. (D-E) The outer radius and aspect ratio measurements of vaterite microspheres grown for 8 h. (F-G) The outer radius and aspect ratio measurements of vaterite microspheres grown for 24 h. Measurements from different stage tilt angles provided insight into the overall external morphology of the entire population.

Understanding the 3D morphology of these microspheres and other similar biomaterials structures across a large population is crucial to determine whether size and morphology can be

modulated by a microbial synthesis approach. From just these three tomographic reconstructions it is clear that there is a variation in the aspect ratio and inner core sizes across the entire population; however, electron tomography is not a high-throughput technique requiring several hours per data acquisition. Automated STEM imaging has been implemented to overcome the bias, variability, and time limitations of typical human operation [36,45], but still only provides 2D projections insufficient to fully characterize complex biomaterials such as our hollow 3D vaterite particles. In order to assess the 3D morphology of a large population of vaterite microspheres, we implemented an automated high-throughput HAADF-STEM imaging method to collect image datasets at several stage tilt angles (-45°, -30°, 0°, 30°, and 45°). A single HAADF-STEM image only shows a 2D projection of the internal structure, but multiple projections at these tilt angles can provide additional morphological information in the third dimension. Further, the full tomographic reconstructions can be used as a basis to infer structural information from a more limited set of tilt angles. HAADF-STEM images were collected from vaterite specimens consisting of microspheres precipitated by the engineered *E. coli* after 8 h and 24 h of growth. The automated high-throughput HAADF-STEM imaging software collected 529 2048 x 2048 images, which is equivalent to a field of view of 360 μm x 360 μm of the sample at 0° tilt with 15 nm resolution as shown in the montage in Figure 4A. Each image was segmented using the workflow shown in Figures 4B and C, and the radii and aspect ratios of the 2D projections of many individual vaterite microspheres were then measured and summarized in the kernel density plots shown in Figures 4D-G and the 2D histograms shown in Figure 5. For the 8 h sample, 1,356 vaterite microspheres were segmented from the HAADF-STEM images after fragments, non-circular precipitates, and clusters of particles were discarded. The mean radius of the 8 h sample is 528 nm with a standard deviation of 111 nm and the mean aspect ratio, which is the ratio of the major axis to the minor axis, is 1.26 with a standard deviation of 0.15. For the 24 h sample, 1,089 microspheres are segmented; the mean radius of the population is 975 nm with a standard deviation of 200 nm and the mean aspect ratio is 1.18 with a standard deviation of 0.10. Furthermore, the average core sizes, which also reveal the shell thickness, were measured using the 2D projection images and the methods described in Section 2.5. The average core size is 206 nm for the 8 h sample and 381 nm for the 24 h sample. Surprisingly, the ratio of the inner radius of the core and the outer radius of the spheres is approximately 1:2.5 as shown in Figures 5A and B, and this ratio holds across the 8 h and 24 h growth time points even though the mean outer diameter of the spheres increases with time.

The same measurements were performed at different stage tilts. The overall size and morphology distributions show that the 8 h sample has more variation with respect to the angular orientation whereas the 24 h sample has relatively similar distributions across the different stage tilts. For the 8 h sample, the difference between the lowest mean value (438 nm, 45° stage tilt) and highest mean value (528 nm, 0° stage tilt) is about 20%. On the other hand, this difference is only about 5% when comparing the lowest mean value (929 nm, -45° stage tilt) to the highest mean value (975 nm, 0° stage tilt). In addition, the median values of microsphere radius and aspect ratio corresponding to each tilt angle are indicated in the kernel density plots shown in Figure 4D-G. The 8 h sample has a much greater spread in the median size measurement than the 24 h sample, showing that the 8 h microspheres are more ellipsoidal than spherical as smaller size deviations between different 2D projections would be associated with the latter. A sphere looks round from any angle whereas a 3D ellipsoid will change its projected shape when viewed from a different direction.

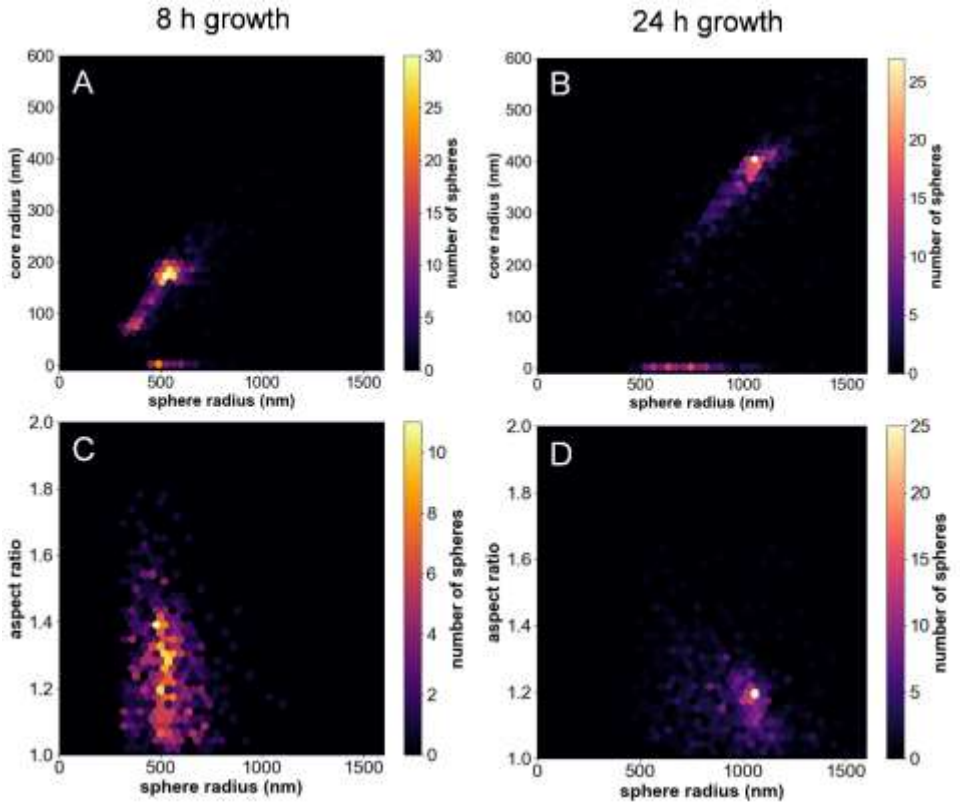

Figure 5. 2D histograms showing the relationships between core radius and aspect ratio of each vaterite microsphere with its outer radius. Vaterite microspheres grown for (A) 8 h and (B) 24 h mostly consist of hollow cores that are 2.5 times smaller than their external size; however, about 12% of the microspheres are solid (no cores). As the microspheres grew larger, the size of the hollow cores grew proportionally. (C) The aspect ratio distribution for the 8 h vaterite microspheres is spread out while (D) the 24 h vaterite microspheres have a much narrower aspect ratio distribution.

The results in Figure 5 show that the vaterite microspheres that were precipitated for 8 h are on average approximately half the size of the ones that were precipitated for 24 h. Moreover, the median radius of the 8 h microspheres changes to a larger degree across the different angular projections than the 24 h microspheres, indicating that the smaller particles are ellipsoidal rather than spherical. Even though both the 8 h and 24 h microspheres both contain many measurements in the range of 1.00 to 1.20, the aspect ratio distribution in the 8 h sample is much broader as about 20% of the measurements fall in between the 1.30 to 1.60 range. This variation in the distribution can be attributed to the changes in the 2D projections of an ellipsoid as it is viewed from different angles. We will describe this in more detail using our experimental data later.

The large-scale HAADF-STEM imaging also reveals that the hollow cores have varying sizes and remarkably, some microspheres do not have hollow centers at all. According to the histograms shown in Figure 5, solid microspheres tend to account for about 12% of the total number of measurements and are typically below average in size. Microbial precipitated solid microspheres have been previously observed [35]; however how a precipitate grows as a hollow or solid microsphere remains an open question. One possible explanation is that urease activity, which influences the amount of CO_2 supplied by the bacterial urea hydrolysis, can modulate the supersaturations in the solution and ultimately the kinetics of $CaCO_3$ formation and the morphology of the crystal precipitates. The relationship between urease activity and 3D precipitate morphology will be discussed elsewhere. Nevertheless, the statistical information of the shape of the microspheres indicates that the 24 h sample has a much narrower aspect ratio distribution. This suggests that as the crystals grow in the *E. coli* culture media, the microspheres become rounder as they increase in size and the hollow core also grows proportional to the overall microsphere size. Furthermore, as illustrated in the 24 h microsphere population in Figures 4F and 5, there is a threshold size of around 1.2 μm in radius as very few measurements exceed this value. This finding suggests that the morphology of vaterite microspheres can be modulated by microbial precipitation in the presence of proteins, demonstrating that biomolecule additives and extracellular organics produced by bacteria can synergistically control the 3D morphology of $CaCO_3$ precipitates. Future studies will investigate the role of different biomolecules and peptides in the production of vaterite microspheres.

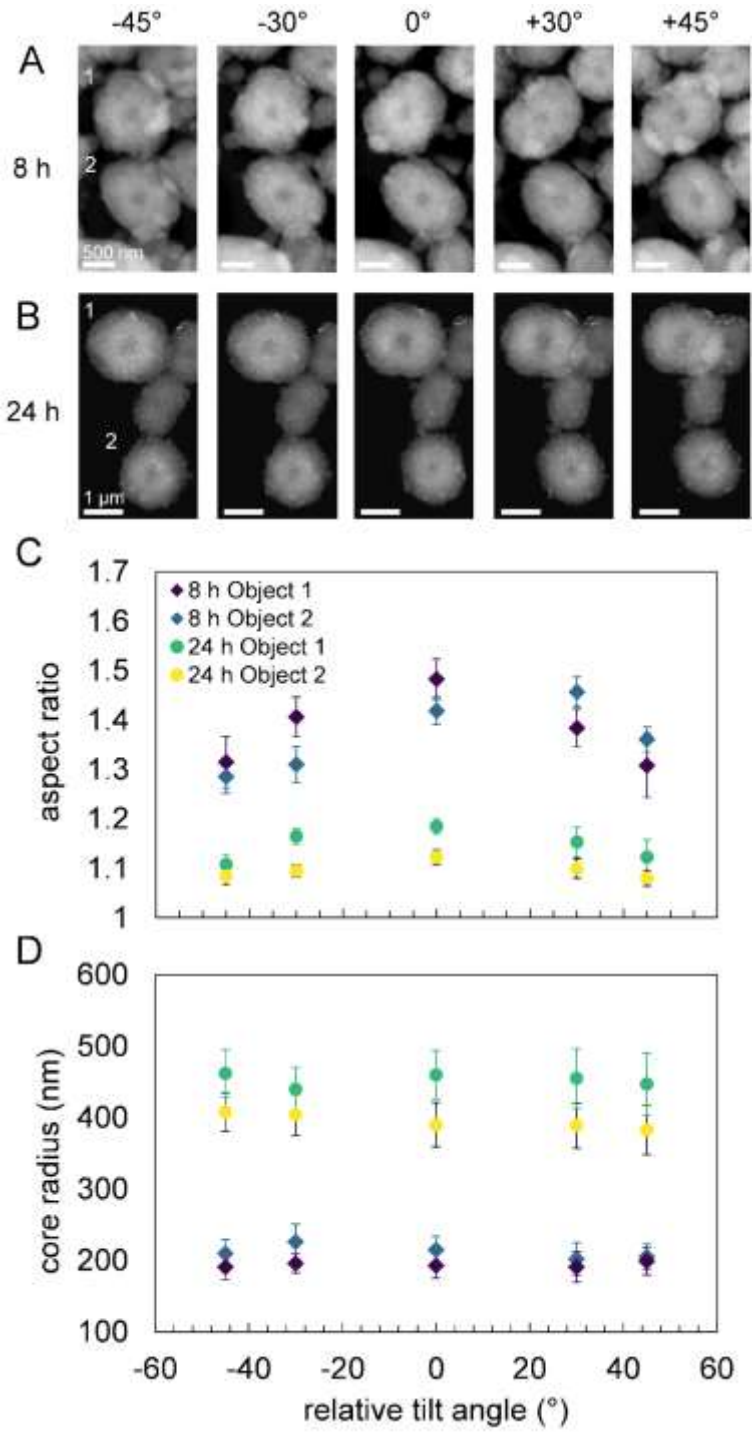

Figure 6. Direct correlation of same vaterite microspheres across five different stage tilts. Two representative microspheres grown for (A) 8 h and (B) 24 h and their 2D projections are shown. These representative microspheres have minimal overlap with neighboring structures, allowing for them to be segmented from the HAADF-STEM images. (C) The change in aspect ratio across different projection angles supports that the 8h microspheres are ellipsoidal and the 24 h microspheres are more spherical. (D) The hollow core radius measurements remain approximately the same across the different projections, indicating that these cavities are spherical regardless of their outer surface morphology.

Finally, the data collected by our non-destructive, automated technique allows us to understand the 3D morphology of many unique single particles beyond the ensemble measurements shown in Figures 4 and 5 by directly correlating the same objects across the five different angular tilts. The 2D cross-correlation method across the five data sets for each time point successfully identified 85 microspheres from the 8 h sample and 51 microspheres from the 24 h sample. Several representative microspheres and their 2D projections are selected and shown in Figure 6. These aspect ratio measurements support the observation that microspheres with a more ellipsoidal morphology have larger fluctuations in both projected outer diameter and aspect ratio between the different projections. At 0° stage tilt, the ellipsoidal microspheres such as the ones commonly observed in the 8 h sample typically have higher aspect ratios. This is due to the fact that an elongated 3D object is more likely to lie on the substrate parallel to its long axis, as the surface area is greater in that orientation. As the stage is tilted, the aspect ratio of the particle's 2D projection will change assuming that the tilt axis is not perfectly aligned with its long axis. Microspheres that are more spherical, as observed in the 24 h microspheres shown in Figure 6, tend to have smaller fluctuations as the aspect ratio of a spherical object will remain fairly constant across different projection angles. Lastly, each 2D projection is a HAADF-STEM image with mass-thickness contrast, thereby allowing the sizes of the hollow cavity to be measured.

As discussed previously by Rodriguez-Navarro *et al.* [34], hollow vaterite microspheres that are formed biotically in the presence of bacteria may or may not encapsulate the bacteria cell. To determine whether *E. coli* cells were encapsulated in the vaterite microspheres, we used the projected core size measurements as mineralized structures that encapsulate bacteria cells typically have oblong cavities [46]. In all of the cases shown in Figure 6, the core size remains approximately the same across the different projections. This indicates that the hollow cavity, which has an irregular rough surface at the nanoscale (Figure 3C), is approximately spherical in each microsphere. These results are strong evidence that the vast majority of these hollow vaterite microspheres do not have an elongated cavity regardless of their outer surface morphology, suggesting that the mineralized structures are not encapsulating the bacteria (which would be ellipsoidal) during the precipitation process. Finally, our HAADF-STEM and STEM-EDX mapping measurements in Figure 2 did not identify any material inside the cavity providing further evidence they are truly hollow. We demonstrated that the microbial synthesis method we used can form vaterite microspheres that have completely empty cavities, enabling the sustainable facile production of these structures for biomedical applications.

There are several limitations to this study. Our TEM samples were not optimized for the tilting experiment, as the overlap of many vaterite microspheres in the sample resulted in fewer segmented objects and morphology measurements. We instead prioritized getting a higher number of measurements at zero-degree tilt to measure core and shell thickness across a large population. Another limitation is that the cubic fitting function used to approximate sizes of the hollow cores does not quantitatively capture the exact projected hollow sphere core radius. As HAADF-STEM image contrast is sensitive to particle overlap artifacts, it was difficult to fit an exact function that can accurately measure the hollow sphere core sizes, and the cubic function fitting method approximated the value while capturing the trends of the inner dimensions of the spheres. Using samples with optimized particle densities on the substrate and a more robust AI/ML approach to segment and correlate these objects, we are confident that we can more quantitatively assess the 3D nanostructure of many more biogenic crystals synthesized using many different growth conditions such as time, temperature, protein additives, and bacteria strains.

4. Conclusions

We used an *E. coli* strain engineered with a urease gene cluster from *S. pasteurii* to produce hollow vaterite microspheres. Using 3D HAADF-STEM tomography, we examined the nanoscale internal structure of several hollow microspheres and revealed that they contain approximately spherical cores with irregular rough surfaces. In order to collect statistical 3D morphology data, which is critical for determining the potential applications of these microspheres, we collected large-scale HAADF-STEM images that contain over 1,000 microspheres across a 360 μm x 360 μm area at 15 nm resolution. We repeated these measurements at five tilt angles to extract large-scale 3D information. By comparing the morphology of the vaterite microspheres at 8 h and 24 h of microbial precipitation, we show that the microspheres evolved from a smaller more ellipsoidal shape to a larger more spherical shape while the internal hollow core increased in size and remained relatively spherical. We demonstrated that 3D electron tomography when combined with high-throughput HAADF-STEM imaging at several different projection angles can be an efficient method to understand the statistical 3D morphology of biomaterials or other materials systems that contain a hollow shell structure.

Declaration of Competing Interest

The authors declare that they have no known competing financial interests or personal relationships that could have appeared to influence the work reported in this paper.

Acknowledgements

This work was supported by the Laboratory Directed Research and Development program (LDRD) at Lawrence Berkeley National Laboratory. This work was partially funded by the US Department of Energy in the program "4D Camera Distillery: From Massive Electron Microscopy Scattering Data to Useful Information with AI/ML." Work at the Molecular Foundry was supported by the Office of Science, Office of Basic Energy Sciences, of the U.S. Department of Energy under Contract No. DE-AC02-05CH11231. Work conducted by the U.S. Department of Energy Joint Genome Institute, a DOE Office of Science User Facility, is supported by the Office of Science of the U.S. Department of Energy operated under Contract No. DE-AC02-05CH11231.

Author Contributions

Alex Y. W. Lin: Conceptualization, Methodology, Software, Investigation, Formal analysis, Writing – original draft, Writing – review & editing. **Zong-Yen Wu:** Methodology, Investigation, Resources. **Alexander J. Pattison:** Software, Validation, Writing – review & editing. **Isaak E. Müller**: Methodology, Investigation, Resources. **Yasuo Yoshikuni:** Supervision, Project administration, Funding acquisition, Writing – review & editing. **Wolfgang Theis:** Methodology, Software, Formal analysis, Visualization, Writing – review & editing. **Peter Ercius:** Conceptualization, Methodology, Funding acquisition, Project administration, Supervision, Formal analysis, Writing – original draft, Writing – review & editing.

References

[1] H.A. Lowenstam, S. Weiner, On Biomineralization, Oxford University Press, 1989.
[2] B.V. Parakhonskiy, A. Haase, R. Antolini, Sub-micrometer vaterite containers: synthesis, substance loading, and release, Angew. Chem. Int. Ed Engl. 51 (2012) 1195–1197. https://doi.org/10.1002/anie.201104316.
[3] S. Donatan, A. Yashchenok, N. Khan, B. Parakhonskiy, M. Cocquyt, B.-E. Pinchasik, D. Khalenkow, H. Möhwald, M. Konrad, A. Skirtach, Loading Capacity versus Enzyme Activity in Anisotropic and Spherical Calcium Carbonate Microparticles, ACS Appl. Mater. Interfaces. 8 (2016) 14284–14292. https://doi.org/10.1021/acsami.6b03492.
[4] D.B. Trushina, T.V. Bukreeva, M.V. Kovalchuk, M.N. Antipina, $CaCO_3$ vaterite microparticles for biomedical and personal care applications, Mater. Sci. Eng. C Mater. Biol. Appl. 45 (2014) 644–658. https://doi.org/10.1016/j.msec.2014.04.050.
[5] D.B. Trushina, T.N. Borodina, S. Belyakov, M.N. Antipina, Calcium carbonate vaterite particles for drug delivery: Advances and challenges, Materials Today Advances. 14 (2022) 100214. https://doi.org/10.1016/j.mtadv.2022.100214.

[6] A. Vikulina, D. Voronin, R. Fakhrullin, V. Vinokurov, D. Volodkin, Naturally derived nano- and micro-drug delivery vehicles: halloysite, vaterite and nanocellulose, New J. Chem. 44 (2020) 5638–5655. https://doi.org/10.1039/C9NJ06470B.
[7] J. Nakamura, G. Poologasundarampillai, J.R. Jones, T. Kasuga, Tracking the formation of vaterite particles containing aminopropyl-functionalized silsesquioxane and their structure for bone regenerative medicine, J. Mater. Chem. B Mater. Biol. Med. 1 (2013) 4446–4454. https://doi.org/10.1039/c3tb20589d.
[8] R. Schröder, L. Besch, H. Pohlit, M. Panthöfer, W. Roth, H. Frey, W. Tremel, R.E. Unger, Particles of vaterite, a metastable CaCO3 polymorph, exhibit high biocompatibility for human osteoblasts and endothelial cells and may serve as a biomaterial for rapid bone regeneration, J. Tissue Eng. Regen. Med. 12 (2018) 1754–1768. https://doi.org/10.1002/term.2703.
[9] P. Wang, T. Shen, X. Li, Y. Tang, Y. Li, Magnetic Mesoporous Calcium Carbonate-Based Nanocomposites for the Removal of Toxic Pb(II) and Cd(II) Ions from Water, ACS Appl. Nano Mater. 3 (2020) 1272–1281. https://doi.org/10.1021/acsanm.9b02036.
[10] P.-Y. Lin, H.-M. Wu, S.-L. Hsieh, J.-S. Li, C. Dong, C.-W. Chen, S. Hsieh, Preparation of vaterite calcium carbonate granules from discarded oyster shells as an adsorbent for heavy metal ions removal, Chemosphere. 254 (2020) 126903. https://doi.org/10.1016/j.chemosphere.2020.126903.
[11] A. Hall, J.D. Taylor, The occurrence of vaterite in gastropod egg-shells, Mineral. Mag. 38 (1971) 521–522. https://doi.org/10.1180/minmag.1971.038.296.17.
[12] H.A. Lowenstam, D.P. Abbott, Vaterite: a mineralization product of the hard tissues of a marine organism (Ascidiacea), Science. 188 (1975) 363–365. https://doi.org/10.1126/science.1118730.
[13] E. Ros, S. Navarro, I. Fernández, M. Reixach, J.M. Ribó, J. Rodés, Utility of biliary microscopy for the prediction of the chemical composition of gallstones and the outcome of dissolution therapy with ursodeoxycholic acid, Gastroenterology. 91 (1986) 703–712. https://doi.org/10.1016/0016-5085(86)90642-6.
[14] R. Lakshminarayanan, E.O. Chi-Jin, X.J. Loh, R.M. Kini, S. Valiyaveettil, Purification and characterization of a vaterite-inducing peptide, pelovaterin, from the eggshells of Pelodiscus sinensis (Chinese soft-shelled turtle), Biomacromolecules. 6 (2005) 1429–1437. https://doi.org/10.1021/bm049276f.
[15] E.R. DuFresne, A. Edward, On the retention of primordial noble gases in the Pesyanoe meteorite, Geochim. Cosmochim. Acta. 26 (1962) 251–262. https://doi.org/10.1016/0016-7037(62)90015-7.
[16] G.M. Friedman, D.J. Schultz, Precipitation of vaterite (CaCO3) during oil field drilling, Mineral. Mag. 58 (1994) 401–408. https://doi.org/10.1180/minmag.1994.058.392.05.
[17] S.E. Grasby, Naturally precipitating vaterite (μ-CaCO3) spheres: unusual carbonates formed in an extreme environment, Geochim. Cosmochim. Acta. 67 (2003) 1659–1666. https://doi.org/10.1016/S0016-7037(02)01304-2.
[18] H. Kawaguchi, H. Hirai, K. Sakai, S. Sera, T. Nakajima, Y. Ebisawa, K. Koyama, Crystallization of inorganic compounds in polymer solutions. Part I: Control of shape and form of calcium carbonate, Colloid Polym. Sci. 270 (1992) 1176–1181. https://doi.org/10.1007/BF01095057.
[19] C.-L. Yao, W.-H. Xu, A.-M. Ding, J.-M. Zhu, Sucrose/bovine serum albumin mediated biomimetic crystallization of calcium carbonate, J. Chem. Sci. . 121 (2009) 89–93. https://doi.org/10.1007/s12039-009-0010-2.
[20] X. Wang, R. Kong, X. Pan, H. Xu, D. Xia, H. Shan, J.R. Lu, Role of ovalbumin in the stabilization of metastable vaterite in calcium carbonate biomineralization, J. Phys. Chem. B. 113 (2009) 8975–8982. https://doi.org/10.1021/jp810281f.
[21] J. Feng, G. Wu, C. Qing, Biomimetic synthesis of hollow calcium carbonate with the

existence of the agar matrix and bovine serum albumin, Mater. Sci. Eng. C Mater. Biol. Appl. 58 (2016) 409–411. https://doi.org/10.1016/j.msec.2015.09.005.
[22] Y. Liu, Y. Chen, X. Huang, G. Wu, Biomimetic synthesis of calcium carbonate with different morphologies and polymorphs in the presence of bovine serum albumin and soluble starch, Mater. Sci. Eng. C Mater. Biol. Appl. 79 (2017) 457–464. https://doi.org/10.1016/j.msec.2017.05.085.
[23] G. Falini, S. Albeck, S. Weiner, L. Addadi, Control of Aragonite or Calcite Polymorphism by Mollusk Shell Macromolecules, Science. 271 (1996) 67–69. https://doi.org/10.1126/science.271.5245.67.
[24] H. Cölfen, M. Antonietti, Crystal Design of Calcium Carbonate Microparticles Using Double-Hydrophilic Block Copolymers, Langmuir. 14 (1998) 582–589. https://doi.org/10.1021/la970765t.
[25] E.M. Pouget, P.H.H. Bomans, J.A.C.M. Goos, P.M. Frederik, G. de With, N.A.J.M. Sommerdijk, The initial stages of template-controlled CaCO3 formation revealed by cryo-TEM, Science. 323 (2009) 1455–1458. https://doi.org/10.1126/science.1169434.
[26] Q.-S. Wu, D.-M. Sun, H.-J. Liu, Y.-P. Ding, Abnormal Polymorph Conversion of Calcium Carbonate and Nano-Self-Assembly of Vaterite by a Supported Liquid Membrane System, Cryst. Growth Des. 4 (2004) 717–720. https://doi.org/10.1021/cg034247u.
[27] Y. Boyjoo, V.K. Pareek, J. Liu, Synthesis of micro and nano-sized calcium carbonate particles and their applications, J. Mater. Chem. A Mater. Energy Sustain. 2 (2014) 14270–14288. https://doi.org/10.1039/C4TA02070G.
[28] Y.S. Han, G. Hadiko, M. Fuji, M. Takahashi, Effect of flow rate and CO2 content on the phase and morphology of CaCO3 prepared by bubbling method, J. Cryst. Growth. 276 (2005) 541–548. https://doi.org/10.1016/j.jcrysgro.2004.11.408.
[29] Ç.M. Oral, B. Ercan, Influence of pH on morphology, size and polymorph of room temperature synthesized calcium carbonate particles, Powder Technol. 339 (2018) 781–788. https://doi.org/10.1016/j.powtec.2018.08.066.
[30] S. Stocks-Fischer, J.K. Galinat, S.S. Bang, Microbiological precipitation of CaCO3, Soil Biol. Biochem. 31 (1999) 1563–1571. https://doi.org/10.1016/S0038-0717(99)00082-6.
[31] L. Liang, C. Heveran, R. Liu, R.T. Gill, A. Nagarajan, J. Cameron, M. Hubler, W.V. Srubar 3rd, S.M. Cook, Rational Control of Calcium Carbonate Precipitation by Engineered Escherichia coli, ACS Synth. Biol. 7 (2018) 2497–2506. https://doi.org/10.1021/acssynbio.8b00194.
[32] C.M. Heveran, L. Liang, A. Nagarajan, M.H. Hubler, R. Gill, J.C. Cameron, S.M. Cook, W.V. Srubar 3rd, Engineered Ureolytic Microorganisms Can Tailor the Morphology and Nanomechanical Properties of Microbial-Precipitated Calcium Carbonate, Sci. Rep. 9 (2019) 14721. https://doi.org/10.1038/s41598-019-51133-9.
[33] K. Ben Chekroun, C. Rodríguez-Navarro, M.T. González-Muñoz, J.M. Arias, G. Cultrone, M. Rodríguez-Gallego, Precipitation and Growth Morphology of Calcium Carbonate Induced by Myxococcus Xanthus: Implications for Recognition of Bacterial Carbonates, J. Sediment. Res. 74 (2004) 868–876. https://doi.org/10.1306/050504740868.
[34] C. Rodriguez-Navarro, C. Jimenez-Lopez, Bacterially mediated mineralization of vaterite, Geochimica et Cosmochimica Acta. (2007). https://doi.org/10.1016/j.gca.2006.11.031.
[35] N.M. Zambare, N.Y. Naser, R. Gerlach, C.B. Chang, Mineralogy of microbially induced calcium carbonate precipitates formed using single cell drop-based microfluidics, Sci. Rep. 10 (2020) 17535. https://doi.org/10.1038/s41598-020-73870-y.
[36] M. Olszta, D. Hopkins, K.R. Fiedler, M. Oostrom, S. Akers, S.R. Spurgeon, An Automated Scanning Transmission Electron Microscope Guided by Sparse Data Analytics, Microsc. Microanal. (2022) 1–11. https://doi.org/10.1017/S1431927622012065.
[37] A.J. Pattison, C.C.S. Pedroso, B.E. Cohen, J. Ondry, P. Alivisatos, W. Theis, P. Ercius, Advanced Techniques in Automated High Resolution Scanning Transmission Electron

Microscopy, Nanotechnology. (2023). https://doi.org/10.1088/1361-6528/acf938.
[38] J. Feng, A.P. Somlyo, A.V. Somlyo, Z. Shao, Automated electron tomography with scanning transmission electron microscopy, J. Microsc. 228 (2007) 406–412. https://doi.org/10.1111/j.1365-2818.2007.01859.x.
[39] J.R. Kremer, D.N. Mastronarde, J.R. McIntosh, Computer visualization of three-dimensional image data using IMOD, J. Struct. Biol. 116 (1996) 71–76. https://doi.org/10.1006/jsbi.1996.0013.
[40] J. Schwartz, C. Harris, J. Pietryga, H. Zheng, P. Kumar, A. Visheratina, N.A. Kotov, B. Major, P. Avery, P. Ercius, U. Ayachit, B. Geveci, D.A. Muller, A. Genova, Y. Jiang, M. Hanwell, R. Hovden, Real-time 3D analysis during electron tomography using tomviz, Nat. Commun. 13 (2022) 4458. https://doi.org/10.1038/s41467-022-32046-0.
[41] P. Ercius, M. Boese, T. Duden, U. Dahmen, Operation of TEAM I in a user environment at NCEM, Microsc. Microanal. 18 (2012) 676–683. https://doi.org/10.1017/S1431927612001225.
[42] A. Cai, X. Xu, H. Pan, J. Tao, R. Liu, R. Tang, K. Cho, Direct Synthesis of Hollow Vaterite Nanospheres from Amorphous Calcium Carbonate Nanoparticles via Phase Transformation, J. Phys. Chem. C. 112 (2008) 11324–11330. https://doi.org/10.1021/jp801408k.
[43] W. Wei, G.-H. Ma, G. Hu, D. Yu, T. McLeish, Z.-G. Su, Z.-Y. Shen, Preparation of hierarchical hollow CaCO3 particles and the application as anticancer drug carrier, J. Am. Chem. Soc. 130 (2008) 15808–15810. https://doi.org/10.1021/ja8039585.
[44] Z. Dong, L. Feng, Y. Hao, M. Chen, M. Gao, Y. Chao, H. Zhao, W. Zhu, J. Liu, C. Liang, Q. Zhang, Z. Liu, Synthesis of Hollow Biomineralized CaCO3-Polydopamine Nanoparticles for Multimodal Imaging-Guided Cancer Photodynamic Therapy with Reduced Skin Photosensitivity, J. Am. Chem. Soc. 140 (2018) 2165–2178. https://doi.org/10.1021/jacs.7b11036.
[45] S.R. Spurgeon, C. Ophus, L. Jones, A. Petford-Long, S.V. Kalinin, M.J. Olszta, R.E. Dunin-Borkowski, N. Salmon, K. Hattar, W.-C.D. Yang, R. Sharma, Y. Du, A. Chiaramonti, H. Zheng, E.C. Buck, L. Kovarik, R.L. Penn, D. Li, X. Zhang, M. Murayama, M.L. Taheri, Towards data-driven next-generation transmission electron microscopy, Nat. Mater. 20 (2021) 274–279. https://doi.org/10.1038/s41563-020-00833-z.
[46] W. De Muynck, N. De Belie, W. Verstraete, Microbial carbonate precipitation in construction materials: A review, Ecol. Eng. 36 (2010) 118–136. https://doi.org/10.1016/j.ecoleng.2009.02.006.